**Fig. 4.** cnn is required for nonrandom segregation of mother and daughter centrosomes. (**A**) Summary of the centrosome-positioning pattern in $cnn^{HK21}$ homozygous mutant and control $cnn^{HK21}/+$ GSCs. Daughter centrosomes were labeled by a pulse of GFP-PACT as in Fig. 1B. Only counts of cells in the second cell cycle are shown. (**B** and **C**) Testis tips from cnn males with GSCs in the second cell cycle with misoriented centrosomes (B) or with the mother rather than the daughter centrosome segregated to the opposite side of the GSC (C). Red, γ-tubulin [centrosomes are shown with arrowheads (M, mother; D, daughter)] and Fas III (hub, H); green, GFP-PACT; blue, Vasa (germ cells). Scale bar, 10 μm.

assembled many cell generations earlier. In contrast, the daughter centrosome migrates away from the niche and is inherited by the cell that will initiate differentiation. We postulate that the mother centrosomes in male GSCs may remain anchored to the GSC-niche interface throughout the cell cycle by attachment to astral microtubules connected to the adherens junction, whereas the daughter centrosomes may initially have few associated microtubules and thus can move away from the niche. Microtubule-dependent differential segregation of mother and daughter spindle-pole bodies (equivalent to centrosomes in higher organisms) is observed in budding yeast (13). In cultured vertebrate cells, the centrioles mature slowly over the cell cycle, and the mother centrosomes (containing a mature centriole) attach astral microtubules more effectively and are more stationary than daughter centrosomes in interphase (14). The unusually early separation of centrosomes in interphase male GSCs may provide a way to move the daughter centrosome out of range of the stabilizing influence of the adherens junction complex before it becomes competent to hold a robust microtubule array.

Developmentally programmed anchoring of the mother centrosome may provide a key mechanism to ensure the stereotyped orientation of the mitotic spindle and thus the reliably asymmetric outcome of the male GSC divisions. Although it is tempting to speculate that de-terminants associated with the mother or daughter centrosome may play a role in specifying stem cell or differentiating-cell fates, such determinants are yet to be identified. Rather, the asymmetric inheritance of mother and daughter centrosomes in male GSCs may be a consequence of the cytoskeletal mechanisms that are imposed as part of the stem cell program to anchor one centrosome next to the niche throughout the interphase, ensuring a properly oriented spindle.

**References and Notes**

1. S. J. Morrison, J. Kimble, *Nature* **441**, 1068 (2006).
2. A. Spradling, D. Drummond-Barbosa, T. Kai, *Nature* **414**, 98 (2001).
3. F. M. Watt, B. L. M. Hogan, *Science* **287**, 1427 (2000).
4. A. A. Kiger, D. L. Jones, C. Schulz, M. B. Rogers, M. T. Fuller, *Science* **294**, 2542 (2001).
5. N. Tulina, E. Matunis, *Science* **294**, 2546 (2001).
6. Y. M. Yamashita, D. L. Jones, M. T. Fuller, *Science* **301**, 1547 (2003).
7. M. Martinez-Campos, R. Basto, J. Baker, M. Kernan, J. W. Raff, *J. Cell Biol.* **165**, 673 (2004).
8. Materials and methods are available as supporting material on *Science* Online.
9. W. D. Tracey Jr., X. Ning, M. Klingler, S. G. Kramer, J. P. Gergen, *Genetics* **154**, 273 (2000).
10. T. L. Megraw, L. R. Kao, T. C. Kaufman, *Curr. Biol.* **11**, 116 (2001).
11. D. Vaizel-Ohayon, E. D. Schejter, *Curr. Biol.* **9**, 889 (1999).
12. T. L. Megraw, K. Li, L. R. Kao, T. C. Kaufman, *Development* **126**, 2829 (1999).
13. G. Pereira, T. U. Tanaka, K. Nasmyth, E. Schiebel, *EMBO J.* **20**, 6359 (2001).
14. M. Piel, P. Meyer, A. Khodjakov, C. L. Rieder, M. Bornens, *J. Cell Biol.* **149**, 317 (2000).
15. We thank the Bloomington Stock Center, the Developmental Studies Hybridoma Bank, and R. Lehmann for reagents; the Stanford Cell Science Imaging Facility for assistance in microscopy; Fuller lab members for comments; the Jose Carreras International Leukemia Foundation for a fellowship to Y.M.Y.; and NIH for grant P01 DK53074 to M.T.F.

# Kinetics of Morphogen Gradient Formation

Anna Kicheva,[1,2]* Periklis Pantazis,[1]*† Tobias Bollenbach,[3]‡ Yannis Kalaidzidis,[1,4] Thomas Bittig,[3] Frank Jülicher,[3]§ Marcos González-Gaitán[1,2]§

In the developing fly wing, secreted morphogens such as Decapentaplegic (Dpp) and Wingless (Wg) form gradients of concentration providing positional information. Dpp forms a longer-range gradient than Wg. To understand how the range is controlled, we measured the four key kinetic parameters governing morphogen spreading: the production rate, the effective diffusion coefficient, the degradation rate, and the immobile fraction. The four parameters had different values for Dpp versus Wg. In addition, Dynamin-dependent endocytosis was required for spreading of Dpp, but not Wg. Thus, the cellular mechanisms of Dpp and Wingless spreading are different: Dpp spreading requires endocytic, intracellular trafficking.

Although the molecular and cellular mechanisms controlling morphogen transport have received much attention, many questions remain open (1–7). This might be due in part to the existence of only a few quantitative studies of the steady-state gradients and the kinetics of morphogen transport. To address this, we studied quantitatively two key morphogens during development of the fly wing: Decapentaplegic (Dpp) and Wingless (Wg).

Dpp is produced at the anterior-posterior compartment boundary in the center of the wing imaginal disc of *Drosophila* (8) (Fig. 1, A and B). Dpp spreads nondirectionally, is degraded while spreading, and forms a gradient of concentration in the plane of the wing epithelium (2, 7). Regardless of the actual transport mechanism, these facts imply that Dpp spreading can be captured by the physics of molecules that are produced in a localized source, which generates a current $j_0$ [molecules/($\mu$m × s)] at the source boundary; that are degraded with a rate $k$ (s$^{-1}$); and that spread in a nondirectional manner with an effective diffusion coefficient $D$ ($\mu$m$^2$/s). Thus, the rate of change of Dpp concentration in the *x-y* plane, $C(x,y,t)$, is described by the equation:

$$\partial_t C = D\nabla^2 C - kC + 2j_0\delta(x) \quad (1)$$

where $t$ is time, $x > 0$ is the distance to the source in the target tissue, $\nabla^2$ is the Laplace operator, and $\delta$ is the Dirac delta function [see supporting online material (SOM)].

The steady-state solution for Eq. 1 is a single exponential gradient:

$$C(x) = C_0 e^{-\frac{x}{\lambda}} \quad (2)$$

where the Dpp concentration $C(x)$ depends only on the distance $x$ from the source, the concentration $C_0$ at the source boundary, and the decay length $\lambda$. The decay length corresponds to the distance at which the concentration decays by a factor $1/e$ of $C_0$ [$C(x) = C_0 (1/e)$ at $x = \lambda$]. The shape of the gradient therefore depends on two key parameters: $\lambda$ and $C_0$, which are determined by $D$, $k$, and $j_0$.

In the scenario of nondirectional morphogen spreading with degradation, $\lambda$ in the steady state is related to the diffusion coefficient and the degradation rate by the expression:

$$\lambda = \sqrt{D/k} \quad (3)$$

In turn, $C_0$ depends on the current $j_0$, and on diffusion and degradation, which occur both in the receiving tissue and in the source:

$$C_0 = j_0/\sqrt{Dk} \quad (4)$$

[1]Max Planck Institute of Molecular Cell Biology and Genetics, Pfotenhauer Strasse 108, 01307 Dresden, Germany. [2]Department of Biochemistry and Department of Molecular Biology, Geneva University, Sciences II, Quai Ernest-Ansermet 30, 1211 Geneva 4, Switzerland. [3]Max Planck Institute for the Physics of Complex Systems, Nöthnitzer Strasse 38, 01187 Dresden, Germany. [4]A. N. Belozersky Institute for Physico-Chemical Biology, Moscow State University, Moscow 119899, Russia.

*These authors contributed equally to this work.
†Present address: California Institute of Technology, Pasadena, CA 91125, USA.
‡Present address: Department of Systems Biology, Harvard Medical School, Boston, MA 02115, USA.
§To whom correspondence should be addressed. E-mail: julicher@pks.mpg.de (F.J.); marcos.gonzalez@biochem. unige.ch (M.G.-G.)

Indeed, the experimental Dpp distribution in the target tissue was well described by a single exponential (Fig. 1C) [correlation index $\langle R^2 \rangle = 0.92 \pm 0.05$, $n = 26$] with a decay length $\lambda = 20.2 \pm 5.7$ $\mu$m, corresponding to $7.7 \pm 2.1$ cells (see materials and methods section in SOM).

To measure the kinetic parameters ($D$, $k$, and $j_0$) that determine the steady-state shape (characterized by $\lambda$ and $C_0$) of the Dpp gradient, we developed an experimental strategy based on imaging a functional green fluorescent protein–Dpp fusion (GFP-Dpp) produced at the endogenous wing source (2) and fluorescence recovery after photobleaching (FRAP) (9, 10). The FRAP assay consisted of irreversibly photobleaching the GFP-Dpp fluorescence in a rectangular region of interest (ROI) with dimensions 10 $\mu$m by 200 $\mu$m adjacent to the source (Fig. 1, D to K). Subsequently, we monitored the fluorescence recovery in the ROI for about 60 min, which

occurred at the expense of the nonbleached GFP-Dpp molecules in the neighboring areas, until the fluorescence intensity was close to a plateau (Fig. 1L). To quantify the recoveries, we imaged and projected five z-confocal planes encompassing the most apical 5 $\mu$m of the epithelium and measured the average fluorescence intensity of GFP-Dpp in the ROI (see materials and methods and fig. S3).

We first controlled several conditions: (i) we limited photodamage and photobleaching during imaging so that they were negligible, (ii) we imaged most of the GFP-Dpp molecules in the tissue, (iii) we estimated the detection inaccuracy, and (iv) we calibrated detection of fluorescence intensity to GFP-Dpp concentration by using GFP-tagged rotavirus particles (11). These important controls are summarized in section 2 of the supporting online material and in figs. S1 and S2. After verification of these conditions, we
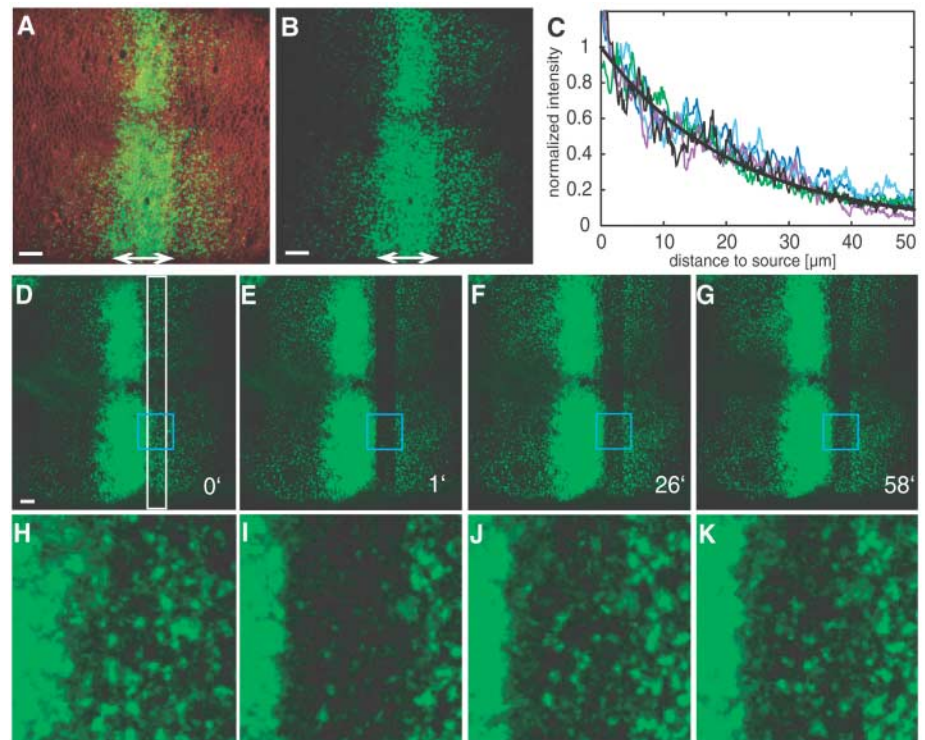


**Fig. 1.** FRAP of GFP-Dpp at 25°C. (**A** and **B**) Wing disc showing GFP-Dpp (green) expressed in the endogenous source (double arrow) with cell profiles counterstained by FM4-64 [red in (A)]. Scale bars, 10 $\mu$m. (**C**) Normalized average fluorescence in the receiving territory of five GFP-Dpp–expressing discs at 25°C as a function of the distance to the source. Black curve, exponential fit to the black trace. (**D** to **G**) FRAP time-lapse images of GFP-Dpp. Projections of five z-sections immediately before (D), immediately after bleaching (E), and during the recovery phase (F and G). Scale bar, 10 $\mu$m. Times (1, 26, 58) indicate minutes after the start of the experiment. White box, ROI. Blue boxes are magnified in (**H** to **K**). (**L**) FRAP recovery curves for four GFP-Dpp experiments at 25°C. Theoretical curves (solid lines) are fit to normalized average fluorescence intensities in the ROI (squares and crosses). Anterior, left. Genotype: *dppGal4::UAS-GFP-Dpp/+*.
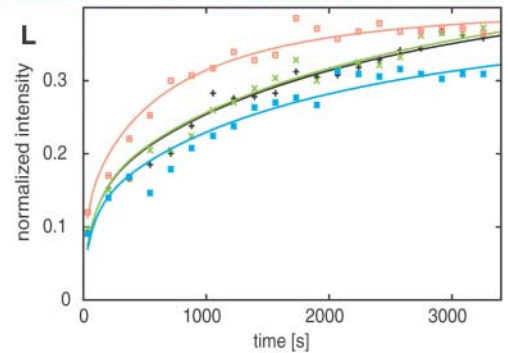
used our calibrations to estimate the concentration of GFP-Dpp at the source boundary $C_0 = 802 \pm 312$ molecules/$\mu m^2$ ($n = 8$ discs), which corresponds to $4379 \pm 1741$ molecules per cell (see materials and methods). In addition, we estimated the fraction of "extracellular" GFP-Dpp, which was equal to or smaller than $15 \pm 3.4\%$ ($n = 8$ discs) of the total pool. The latter measurement, together with the fact that our detection inaccuracy was less than 2%, showed that the extracellular pool was not a dominant pool (section 2 of SOM).

We then studied the recovery profiles in the FRAP experiments to determine $D$, $k$, and $j_0$, as well as the immobile fraction $\psi$. $\psi$ is the fraction of molecules that did not recover in the ROI during the experiment. The standard procedure (12) to solve the diffusion equation, which neglects production and degradation and is commonly used in FRAP studies of single cells (13), is not suitable for our FRAP assay in tissues. The time span of recovery in tissue FRAP was 30 to 90 min (Fig. 1), so that production and degradation could not be neglected. Thus, we solved Eq. 1 for the particular geometry and conditions of our FRAP experiments in the tissue (SOM, fig. S3D).

From the resulting time-dependent concentration profile $C(x,y,t)$ (fig. S3D), we calculated the average concentration $f(t)$ in the ROI as a function of time. We optimized the two parameters $D$ and $\psi$, which determine the shape of this theoretical recovery curve, to obtain the best agreement with the experimental curves (see SOM). The parameters $k$ and $j_0$ were not independent, because we measured two key quantities before bleaching that impose further constraints: (i) the decay length $\lambda$, which allows

us to determine $k$ from the fitted $D$ via Eq. 3: $\lambda = \sqrt{D/k}$, and (ii) the concentration at the source boundary $C_0$, which enabled us to determine $j_0$ via Eq. 4: $C_0 = j_0/\sqrt{Dk}$. The resulting theoretical curves were in excellent agreement with the experimental recovery data ($R^2 = 0.95 \pm 0.03$) (see also table S1), which provided sufficient constraints to confidently determine the actual values of $D$ and $\psi$. Thus, analysis of the experimental recovery curves, together with Eqs. 3 and 4, allowed us to determine the kinetic parameters $D$, $k$, $j_0$, and $\psi$ of morphogen spreading.

The effective diffusion coefficient of GFP-Dpp was $D = 0.10 \pm 0.05$ $\mu m^2/s$ ($n = 8$ experiments). This number is about three orders of magnitude less than the coefficient of free diffusion in water of molecules with the size of the mature Dpp homodimer [similar to that of GFP, which has $D = 87$ $\mu m^2/s$ (14)], but consistent with (i) restricted diffusion of Dpp in the extracellular space [e.g., hindered by binding to immobile extracellular matrix molecules or membrane receptors (15–17)] and (ii) endocytosis plus recycling of Dpp through a fast recycling pathway (18). Dpp was degraded at a rate $k = 2.52 \times 10^{-4} \pm 1.29 \times 10^{-4}$ s$^{-1}$ corresponding to a GFP-Dpp half-life of about 45 min, which is consistent with the turnover time of Dpp molecules in the developing wing determined biochemically (7). In addition, the majority of the GFP-Dpp molecules in the target tissue were immobile or moved very slowly ($\psi = 62 \pm 8\%$), i.e., with recovery kinetics too slow compared with the 60-min time scale of the FRAP experiments. This immobile pool was stored in intracellular compartments, because the extracellular pool was equal to or smaller than 15% of
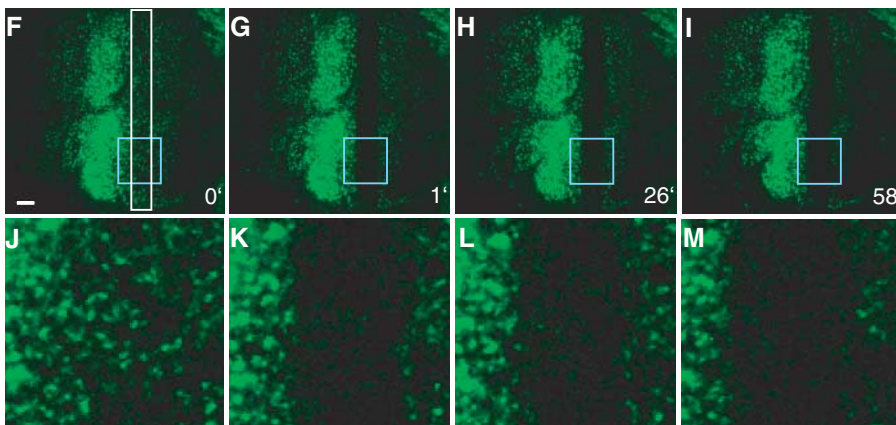
the total pool. We found $j_0 = 3.98 \pm 2.34$ molecules/($\mu m \times s$), which implies that the Gal4-driven GFP-Dpp production rate from the endogenous source was $\nu = 2.69 \pm 1.58$ molecules per cell per second. The effective production rate $\nu$ per cell with diameter $a$ can be obtained from $j_0$ by $\nu \approx 2a^2 j_0/w$ for small values of the width of the source $w$ ($\mu m$) (3).

We tested the validity of the diffusion and degradation description for the FRAP recoveries by performing FRAP experiments in different geometries (fig. S4 and table S1). The results of these experiments were consistent with the independence of the four kinetic parameters on position in the tissue (see SOM).

After studying the GFP-Dpp kinetics, we analyzed the dependence of gradient formation on endocytosis by performing the FRAP assay in animals where the target tissue was mutant for the thermosensitive *shibire*$^{ts1}$ allele and in which the source was rescued by a functional *shibire*$^+$ transgene ["shibire-rescue" animals; see materials and methods and (2)]. The role of endocytosis has previously been studied using shibire-rescue animals in qualitative assays (1, 2) (SOM and fig. S5). The FRAP assay allowed us to determine separately $D$, $k$, $\nu$, and $\psi$ in each experimental condition and to measure sensitively the kinetic effects in conditions of partial or complete endocytic block [in the wing, *shibire*$^{ts1}$ is a tight thermosensitive mutant at 34°C, but leaky at 32°C (2) (fig. S5)]. In addition, during the FRAP experiment, the effects could be detected immediately, after only a few minutes of block. In control animals, $D$, $k$, $\nu$, and $\psi$ were not significantly different at 25°C, 32°C, and 34°C (figs. S6 and S7). In shibire-rescue animals, which were raised at the permissive temperature, the
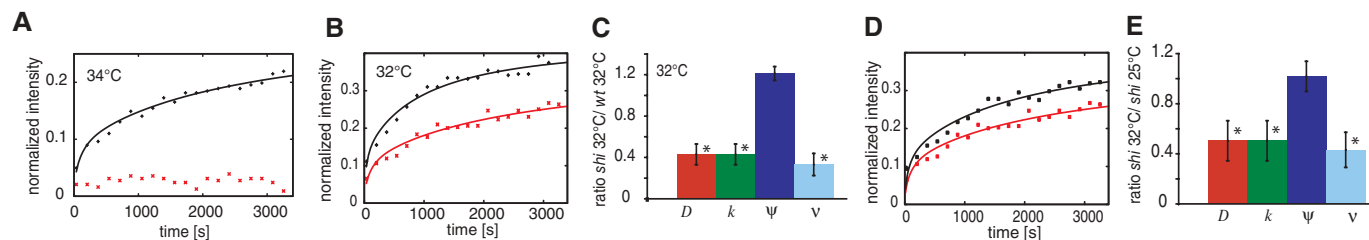


**Fig. 2.** GFP-Dpp shibire-rescue FRAP assay at 32°C and 34°C. (**A** and **B**) FRAP recovery curves of GFP-Dpp (black) and GFP-Dpp shibire rescue (red) at 34°C (A) and 32°C (B). Genotypes: *dppGal4::UAS-GFP-Dpp/+* and *shi$^{ts1}$; UAS-Dynamin$^+$/+; UAS-GFP-Dpp/dppGal4*. (**C**) Average $D$, $k$, $\psi$, and $\nu$ from seven GFP-Dpp shibire-rescue experiments at 32°C normalized to the respective averages at 32°C in GFP-Dpp (wild-type control). Error bars, SEM. Asterisks, statistically significant differences between shibire rescue and wild-type at 32°C (double-sided $P < 0.05$). (**D**) GFP-Dpp shibire rescue at 25°C (black) and 32°C (red). (**E**) Average $D$, $k$, $\psi$, and $\nu$ from eight GFP-Dpp shibire-rescue experiments at 32°C normalized to the respective average in GFP-Dpp shibire rescue at 25°C. Asterisks, statistically significant differences. (**F** to **M**) FRAP time-lapse images of GFP-Dpp shibire rescue at 34°C as in Fig. 1, D to K.

tight endocytic block at 34°C during the FRAP experiment impaired Dpp spreading completely, and no recovery could be detected into the ROI (Fig. 2, A and F to M). When the block was released by shifting the temperature down to 25°C, fluorescence recovered into the ROI, which indicated that the effect was reversible and that the lack of recovery was not due to unspecific tissue damage (fig. S8).

This lack of recovery after the tight endocytic block was imposed could be due to decreased diffusion or increased degradation rate. Because no recovery was observed, a theoretical curve could not be fitted to determine the actual values of the kinetic parameters. Thus, we studied the recoveries under conditions of partial block of endocytosis at 32°C. At 32°C, the diffusion coefficient in shibire-rescued animals decreased by a factor of more than 2 compared with that of control animals at 32°C (Fig. 2, B and C) and with shibire-rescued animals at the permissive temperature 25°C (Fig. 2, D and E, and table S1). The degradation rate was not increased, but decreased by a factor of about 2. Finally, the production rate was also affected, whereas ψ was not (see materials and methods). Thus endocytosis is required not only for Dpp degradation, but also for Dpp movement.

It is worth noting here that (i) given our imprecision of measurement (2%, see SOM), the minimal recovery we would have been able to detect is 2% of the total pool (fig. S2, E to G), excluding the possibility that we might have missed a significant extracellular recovery; (ii) other morphogens did recover in this FRAP shibire-rescue assay, which excludes an intrinsic artifact of the treatment as causing the lack of recovery (see below); (iii) the observed effects of endocytic block were acute, because the lack of recovery was observed after a few minutes of block; and (iv) the endocytic block was reversible.

To explore whether this kinetic description of Dpp applied to other morphogens, we performed the same FRAP analysis for another secreted ligand, Wingless (Wg) (Fig. 3, A to H and J). In order to compare Wg and Dpp, we expressed a functional GFP-Wingless fusion (19) at the endogenous Dpp source, instead of the endogenous source region of Wg in wild type (Fig. 3, A to D). Wg also moves in the tissue nondirectionally and is degraded, but had a different profile (Fig. 3I). The Dpp gradient is a long-range gra-
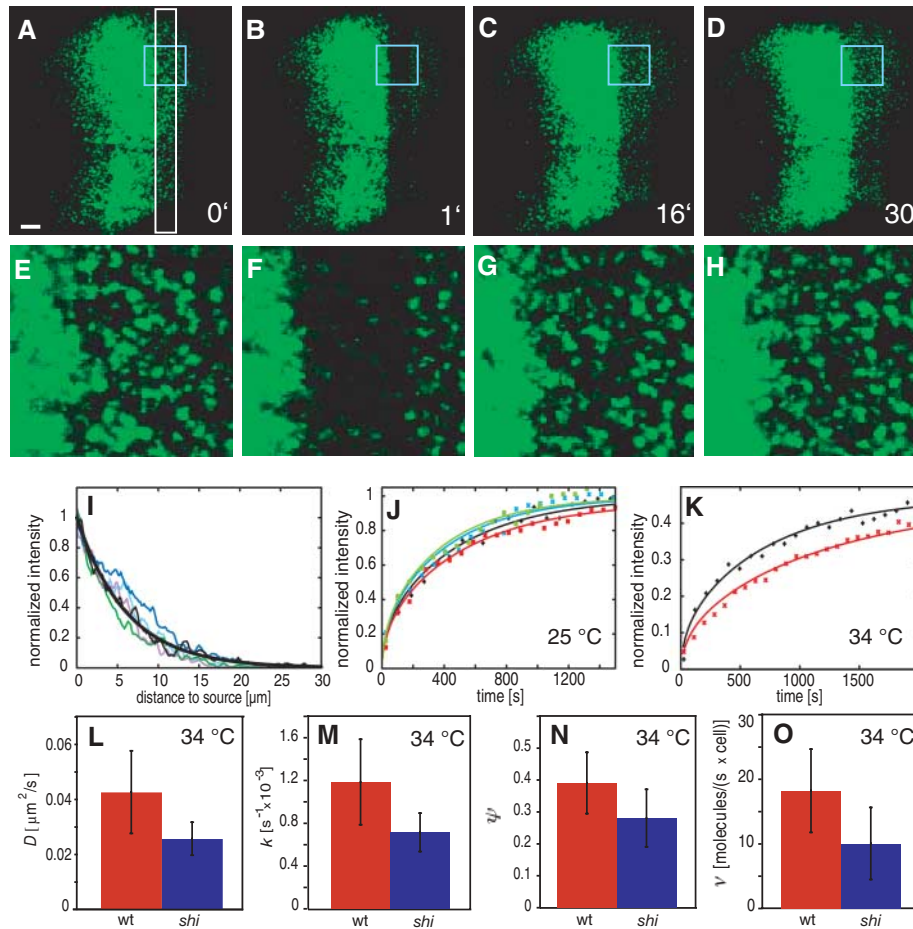


**Fig. 3.** FRAP of GFP-Wingless and GFP-Wingless shibire rescue. (**A** to **H**) FRAP time-lapse images of GFP-Wg expressed in the wing Dpp domain. Boxes and times as in Fig. 1, D to K. Genotype: *UAS-GFP-wingless/+; dppGal4/+*. Scale bar, 10 μm. (**I**) Normalized average fluorescence in the receiving territory of five Wg-expressing discs at 25°C as a function of the distance to the source. Black curve, exponential fit to the black trace. (**J**) Four FRAP recovery traces of GFP-Wingless at 25°C. (**K**) GFP-Wingless (black) and GFP-Wingless shibire rescue at 34°C (red). Genotypes: *UAS-GFP-wingless/+; dppGal4/+* and *shi^ts1; UAS-Dynamin+/UAS-GFP-wingless; dppGal4/+*. (**L** to **O**) Average D, k, ψ, and ν from GFP-Wingless (red; n = 9) and GFP-Wingless shibire-rescue experiments at 34°C (blue; n = 10). Error bars, SEM. The differences are not statistically significant for any of the four parameters considered.
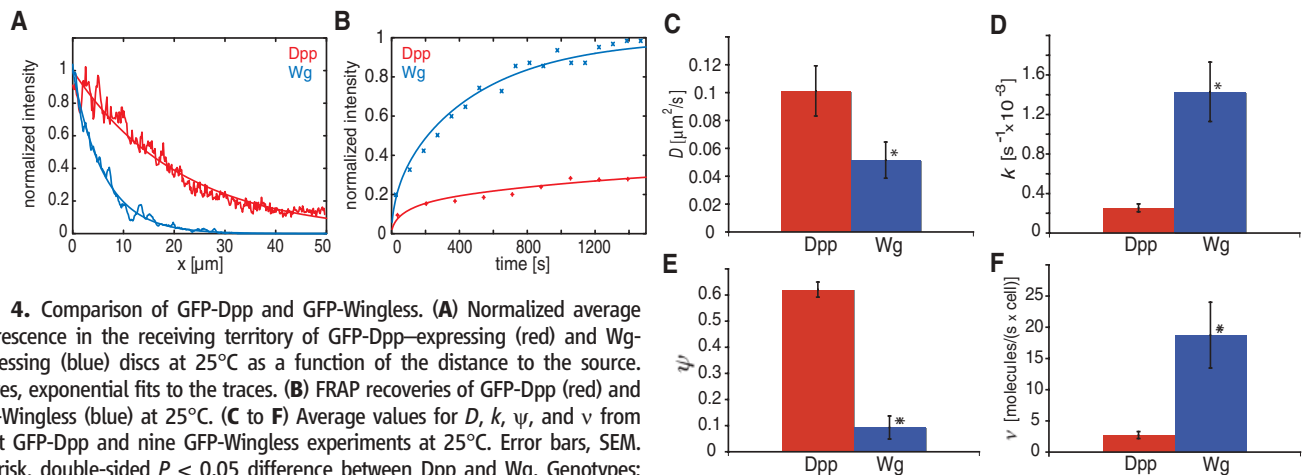


**Fig. 4.** Comparison of GFP-Dpp and GFP-Wingless. (**A**) Normalized average fluorescence in the receiving territory of GFP-Dpp–expressing (red) and Wg-expressing (blue) discs at 25°C as a function of the distance to the source. Curves, exponential fits to the traces. (**B**) FRAP recoveries of GFP-Dpp (red) and GFP-Wingless (blue) at 25°C. (**C** to **F**) Average values for D, k, ψ, and ν from eight GFP-Dpp and nine GFP-Wingless experiments at 25°C. Error bars, SEM. Asterisk, double-sided P < 0.05 difference between Dpp and Wg. Genotypes: *dppGal4::UAS-GFP-Dpp/+* and *UAS-GFP-wingless/+; dppGal4/+*.

dient with decay length λ = 20.2 μm, whereas, in these in vivo conditions, Wg made a short-range gradient with λ = 5.8 ± 2.04 μm (Figs. 3I and 4A). Which kinetic parameter could account for this difference? Because Dpp and Wg have inherently different properties—Wg is a lipid-modified molecule (20); Dpp is not (21)—they are likely to display different mechanisms and kinetics of spreading through the epithelium.

The shorter decay length of the Wingless gradient was due to a higher degradation rate of GFP-Wingless, by a factor of 5, and to a lesser extent its smaller diffusion coefficient (Fig. 4). Although the Gal4 driver was the same in the Dpp and Wg experiments, the production rate of Wg was about seven times that of Dpp, which implied that their maturation and secretion were controlled differently. In addition, while 62% of the Dpp molecules were immobile, the Wg pool was almost fully mobile at 25°C (ψ = 9.2 ± 13%), although, unlike Dpp, a significant immobile fraction appeared at higher experimental temperatures (Fig. 3, K and N). The different immobile fractions of Dpp and Wg at 25°C validated the specificity of the Dpp immobile fraction. Thus, the immobile fraction was not an artifact of incomplete recovery in sick cells. Finally, in contrast to Dpp, Wg transport and degradation were independent of Dynamin endocytosis (Fig. 3, K to O). Indeed, Wg movement has been suggested to be Dynamin-independent (6, 22). In addition, expression of dominant-negative Dynamin

and/or long-term thermosensitive *shibire* block caused an extension of the gradient in the wing (5, 22, 23), which was attributed to decreased degradation (5, 22). Our FRAP approach studying the results of an acute block suggests that endocytosis is not required for Wg transport and degradation or, alternatively, that endocytosis of Wg is Dynamin-independent.

Altogether, the GFP-Wingless FRAP experiments (i) validated our FRAP assay and shibire-rescue experiment; (ii) indicated that different morphogen gradients can be generated by independently fine-tuning D, k, ν, and ψ; and (iii) showed that different morphogens may use different mechanisms of transport and cellular machineries (e.g., Dynamin-dependent versus Dynamin-independent transport) to achieve the formation of morphogen gradients.

### References and Notes

1. T. Y. Belenkaya et al., Cell 119, 231 (2004).
2. E. V. Entchev, A. Schwabedissen, M. González-Gaitán, Cell 103, 981 (2000).
3. K. Kruse, P. Pantazis, T. Bollenbach, F. Jülicher, M. González-Gaitán, Development 131, 4843 (2004).
4. A. D. Lander, Q. Nie, F. Y. Wan, Dev. Cell 2, 785 (2002).
5. E. Piddini, F. Marshall, L. Dubois, E. Hirst, J.-P. Vincent, Development 132, 5479 (2005).
6. M. Strigini, S. M. Cohen, Curr. Biol. 10, 293 (2000).
7. A. A. Teleman, S. M. Cohen, Cell 103, 971 (2000).
8. K. Basler, G. Struhl, Trends Genet. 10, 187 (1994).
9. J. Lippincott-Schwartz, N. Altan-Bonnet, G. H. Patterson, Nat. Cell Biol. 5 (suppl.), S7 (2003).
10. G. Carrero, D. McDonald, E. Crawford, G. de Vries, M. J. Hendzel, Methods 29, 14 (2003).
11. A. Charpilienne et al., J. Biol. Chem. 276, 29361 (2001).
12. D. Axelrod, D. E. Koppel, J. Schlessinger, E. Elson, W. W. Webb, Biophys. J. 16, 1055 (1976).
13. J. Ellenberg, J. Lippincott-Schwartz, Methods 19, 362 (1999).
14. R. Swaminathan, C. P. Hoang, A. S. Verkman, Biophys. J. 72, 1900 (1997).
15. G.-H. Baeg, E. M. Selva, R. M. Goodman, R. Dasgupta, N. Perrimon, Dev. Biol. 276, 89 (2004).
16. C. Han, D. Yan, T. Y. Belenkaya, X. Lin, Development 132, 667 (2005).
17. T. Lecuit, S. M. Cohen, Development 125, 4901 (1998).
18. J. Klingauf, E. T. Kavalali, R. W. Tsien, Nature 394, 581 (1998).
19. S. Pfeiffer, S. Ricardo, J.-B. Manneville, C. Alexandre, J.-P. Vincent, Curr. Biol. 12, 957 (2002).
20. K. Willert et al., Nature 423, 448 (2003).
21. J. Groppe et al., J. Biol. Chem. 273, 29052 (1998).
22. E. S. Seto, H. J. Bellen, J. Cell Biol. 173, 95 (2006).
23. A. F. Rives, K. M. Rochlin, M. Wehrli, S. L. Schwartz, S. DiNardo, Dev. Biol. 293, 268 (2006).
24. We thank J.-P. Vincent and A. Charpilienne for reagents, C. P. Heisenberg and E. Entchev for critical reading of the manuscript, as well as all members of the M.G.-G. and F.J. groups. This work was supported by the Max Planck Society, Deutsche Forchungsgemeinschaft, Volkswagen Stiftung, the European Union, and the Human Frontier Science Program.

# A "Silent" Polymorphism in the *MDR*1 Gene Changes Substrate Specificity

Chava Kimchi-Sarfaty,*† Jung Mi Oh,†‡ In-Wha Kim, Zuben E. Sauna, Anna Maria Calcagno, Suresh V. Ambudkar, Michael M. Gottesman†

Synonymous single-nucleotide polymorphisms (SNPs) do not produce altered coding sequences, and therefore they are not expected to change the function of the protein in which they occur. We report that a synonymous SNP in the *Multidrug Resistance* 1 (*MDR*1) gene, part of a haplotype previously linked to altered function of the *MDR*1 gene product P-glycoprotein (P-gp), nonetheless results in P-gp with altered drug and inhibitor interactions. Similar mRNA and protein levels, but altered conformations, were found for wild-type and polymorphic P-gp. We hypothesize that the presence of a rare codon, marked by the synonymous polymorphism, affects the timing of cotranslational folding and insertion of P-gp into the membrane, thereby altering the structure of substrate and inhibitor interaction sites.

The *MDR*1 gene product, the adenosine triphosphate (ATP)–binding cassette (ABC) transporter ABCB1 or P-gp, is an ATP-driven efflux pump contributing to the pharmacokinetics of drugs that are P-gp substrates and to the multidrug resistance of cancer cells (1, 2). To date, more than 50 single-nucleotide polymorphisms (SNPs) have been reported for *MDR*1 (www.ncbi.nlm.nih.gov/SNP/GeneGt.cgi?geneID=5243). One of these, a synonymous SNP in exon 26 (C3435T), was

sometimes found to be associated with altered P-gp activity (3–6) and, when it appears in a haplotype, with reduced functionality (7). This association may be explained in different ways. Perhaps it is because C3435T is in linkage disequilibrium with other common functional nonsynonymous polymorphisms such as G2677T. In fact, the C1236T (a synonymous SNP), G2677T, and C3435T polymorphisms are part of a common haplotype (8, 9). Another possible explanation is that allele-specific differences in

mRNA folding could influence splicing, processing, or translational control and regulation (10, 11). A third possibility is that the effect of the C3435T polymorphism on the levels of cell surface P-gp activity or its function is rather modest or drug-specific. Finally, numerous environmental factors are known to affect the expression and phenotypic activity of P-gp (12).

To determine whether the C3435T polymorphism actually does affect P-gp activity, we expressed wild-type and polymorphic P-gps in HeLa cells with the use of a transient expression system (13). The same experiments were carried out on BSC-1 (epithelial cells of African green monkey kidney origin), Vero-76 (monkey kidney cells), and 12E1 (CEM human cells) cell lines (14), with similar results, indicating that this phenomenon is not specific to HeLa cells.

Laboratory of Cell Biology, Center for Cancer Research, National Cancer Institute, Bethesda, MD 20892, USA.

*Present address: Center for Biologics Evaluation and Research, Food and Drug Administration, 29 Lincoln Drive, Room 316, Bethesda, MD 20892, USA.
†To whom correspondence should be addressed. E-mail: mgottesman@nih.gov (M.M.G.); jmoh@snu.ac.kr (J.M.O.); kimchi@cber.fda.gov (C.K.-S.)
‡Present address: College of Pharmacy, Seoul National University, Seoul 151-742, South Korea.